Scanning Transmission Electron Microscopy Investigation of Differences in the High Temperature Redox Deactivation Behavior of $CePrO_x$ Particles Supported on Modified Alumina

Miguel López-Haro,[†,‡] Karima Aboussaïd,[†] Juan C. Gonzalez,[†] Juan C. Hernández,[§] José M. Pintado,[†] Ginesa Blanco,[†] José J. Calvino,[†] Paul A. Midgley,[§] Pascale Bayle-Guillemaud,[‡] and Susana Trasobares*[,†,‡]

Departamento de Ciencia de los Materiales e Ingeniería Metalúrgica y Química Inorgánica, Facultad de Ciencias, Campus Rio San Pedro, Universidad de Cádiz, Puerto Real, 11510-Cádiz, Spain, CEA Grenoble, INAC/SP2M, 17 Rue de Martyres, 38054 Grenoble, France, and Department of Materials Science and Metallurgy, University of Cambridge, Pembroke Street, Cambridge CB2 3QZ, U.K.

Received October 24, 2008. Revised Manuscript Received January 19, 2009

An in-depth structural and analytical investigation of two 25 wt % $Ce_{0.8}Pr_{0.2}O_2$/d-Al_2O_3 catalysts, d = 3.5 wt % SiO_2, 4 wt % La_2O_3, is performed aimed at clarifying the origin of the differences in the evolution of their oxygen storage capacity with temperature. Using a combination of transmission and scanning transmission electron microscopy techniques, the fine details of the structural and compositional changes of the two catalysts with reduction temperature has allowed us to establish the role of SiO_2 as a stabilizer of the oxygen handling properties of the Ce−Pr mixed oxide phase under high temperature reducing environments. The entire set of data clearly reveals that Pr does not fully mix with Ce during the synthesis of both catalysts, the spatial distribution of this uncombined fraction of Pr loading being in each case very different: as nanosized particles in the catalyst prepared on the SiO_2-doped substrate and as a highly dispersed phase in the lanthana modified alumina catalyst. Therefore, SiO_2 doping provides a barrier against lanthanide element incorporation into the alumina support. This effect hinders the formation of large amounts of the $LnAlO_3$ (Ln = Ce, Pr) perovskite phase which, as established by HREM and XRD, is responsible of the loss of oxygen storage capacity during hydrogen treatments at temperatures above 800 °C.

Introduction

$CePrO_x$ mixed oxides, which present redox properties improved with respect to those characteristic of pure ceria (CeO_2), have a wide range of potential applications, spanning from environmental catalysis to nontoxic pigments for industrial ceramics,[1−3] or as cathodes for fuel cells.[4] Within the field of environmental catalysis they have been tested as alternative redox promoters in processes such as three way catalysis (TWC),[5] in low temperature water gas shift (WGS) for hydrogen production, as well as in the catalytic wet air oxidation (CWAO) reaction to abate organic pollutant components present in industrial wastewaters.[6] In all these applications, both the thermodynamics and the kinetics of the exchange of the oxide lattice oxygen with its environment, which are usually quantified in terms of the so-called oxygen storage capacity (OSC), are critical parameters.

The OSC of ceria-based oxides is directly related to their range of nonstoichiometries and the capability of the ceria cation to change valence states, allowing the release and uptake of oxygen.[5,7] The incorporation of metallic alio-cations with smaller valence states (for example La^{3+} or praseodimium, which can eventually be Pr^{3+}) creates extrinsic defects, oxygen vacancies, which enable the migration of oxygen ions through the lattice and provides the material with high levels of nonstoichiometry even under oxidizing conditions. Several authors[8−12] have demonstrated that adding praseodymium oxide into the host lattice of the CeO_2 fluorite structure improves the OSC of the system. Given that praseodymium oxide presents, as CeO_2, a fluorite type structure and also that Ce^{4+} and Pr^{4+} have similar ionic radii, these two oxides form solid solutions in a wide range of compositions. Nauer et al.[9] have demonstrated that the OSC of $CePrO_x$ oxides at low temperature exceeds those observed for pure ceria and pure praseodymium oxide. In the mixed oxide, the Pr ions

[†] Universidad de Cádiz.
[‡] CEA Grenoble.
[§] University of Cambridge.

(1) Rojas, T. C.; Ocana, M. *Scr. Mater.* **2002**, *46* (9), 655–660.
(2) Sulcova, P.; Trojan, M. *Thermochim. Acta* **2003**.
(3) Aruna, S. T.; Ghosh, S.; Patil, K. C. *Int. J. Inorg. Mater.* **2001**, *3* (4−5), 387–392.
(4) Stefanik, T. S.; Teuller, H. L. *J. Electroceram.* **2004**.
(5) Logan, A. D.; Shelef, M. *J. Mater. Res.* **1994**, *9* (2), 468–475.
(6) Mikulova, J.; Rossignol, S.; Barbier, J.; Mesnard, D.; Kappenstein, C.; Duprez, D. *Appl. Catal. B* **2007**, *72* (1−2), 1–10.
(7) Knauth, P.; Tuller, H. L. *J. Eur. Ceram. Soc.* **1999**, *19* (6−7), 831–836.
(8) Brauer, G.; Willaredt, B. *J. Less-Common Met.* **1978**, *61* (1), 83–89.
(9) Nauer, M. C. F. B.; Steele, C. H. *J. Eur. Ceram. Soc.* **1994**, 14.
(10) Kang, Z. C.; Eyring, L. *J. Solid State Chem.* **2000**, *155* (1), 129–137.
(11) Ryan, K. M.; McGrath, J. P.; Farrell, R. A.; O'Neill, W. M.; Barnes, C. J. *J. Phys.: Condens. Matter* **2003**.
(12) Borchert, H.; Frolova, Y. V.; Kaichev, V. V.; , Prosvirin, I. P.; Alikina, G. M.; Lukashevich, V. I.; Zaikovskii, V. I.; Moroz, E. M.; Trukhan, S. N.; Ivanov, V. P.; Paukshtis, E. A.; Bukhtiyarov, V. I.; Sadykov, V. A. *J. Phys. Chem. B* **2005**, *109*, 5728–5738.

10.1021/cm8029054 CCC: $40.75
Published on Web 02/20/2009

can exchange between the trivalent and tetravalent states at milder conditions of temperature and pressure than in pure praseodymia.[5,13]

Thinking of applications in which the key point is the transfer of oxygen from these oxides to other species in the surroundings, as it would be the case of catalytic processes occurring at the oxide-environment interface, the kinetics of the whole process could eventually benefit from a large surface of the oxide. Thus, as long as a decrease in the oxide particle size does not involve a concomitant deterioration of the bulk redox properties, dispersing these mixed oxides on the surface of a carrier support would allow preparing redox promoters with improved performance. Transition aluminas, which provide high surface areas and adequate porosity and at the same time present good mechanical and thermal properties[14] are commonly used as supports for catalytically active phases. Therefore, supporting on alumina would allow improving the redox performance of Ce−Pr mixed oxides.

In most catalytic processes carried out at moderate temperatures, the textural properties of transition aluminas are not affected. However, in those catalytic processes carried out at elevated temperatures or which can eventually suffer from uncontrolled excursions to high temperature conditions, both structural changes and surface area losses of the alumina can take place. Several authors[15−18] have shown that the surface area loss which occurs during the textural transformation of alumina is produced by the condensation of hydroxyl groups and adjacent alumina particles. Nevertheless, the thermal properties of alumina can be improved by adding agents such as lanthanide elements, alkaline earth elements, zirconium, and silicon oxides.[19] Among these, several authors have proved that lanthanum oxide presents one of the best performance as texture stabilizer.[20−22] Using a Cs-corrected scanning transmission electron microscope and first-principles calculations, Wang et al.[23] have demonstrated that the stabilization of the system is achieved by spreading isolated La atoms onto the alumina surface. Likewise, Popa et al.[24] have investigated the use of SiO_2 as an alumina dopant. They have evidenced that the textural stabilization in this case is due to the insertion of Si atoms into the alumina structure. In a recent contribution[25] the OSC of materials with formulation $Ce_{0.8}Pr_{0.2}O_{2-x}/Al_2O_3$-4% La_2O_3 and $Ce_{0.8}Pr_{0.2}O_{2-x}/Al_2O_3$-3.5% SiO_2 was determined for reduction treatments in hydrogen in a wide range of temperatures, 350−900 °C. Although in both materials a deterioration of the OSC values was observed at the highest temperature, the material based on the SiO_2-doped alumina retained a much higher redox activity.

In this paper, high resolution electron microscopy (HREM) and high angle annular dark field (HAADF) have been combined with spectroscopic techniques, like electron energy loss spectroscopy (EELS) and X-ray energy dispersive spectroscopy (X-EDS), to investigate the influence of the nature of these two dopants (SiO_2, La_2O_3) used to stabilize alumina, on the resistance of these materials against redox-activity decay under high temperature aging conditions. Complementary, average, information has been obtained by X-ray photoelectron spectrocopy (XPS) analysis. On the basis of both the atomic-scale and macroscopic views obtained with these techniques we propose a mechanism to explain the differences observed in the decay of redox activity after high temperature reduction treatments.

The results obtained have also allowed us to monitor, with subnanometer resolution, the spatial distribution of the lanthanide elements in the complex alumina-supported $CePrO_x$ materials. In particular, a clear picture of the mixing degree of Ce and Pr in the supported mixed-oxide particles, both in the as-synthesized materials and in the aged ones, has been obtained. This is possibly a key issue to rationalize the redox behavior of these materials which intend to exploit the synergy between the two reducible lanthanide elements. In this respect, the data included in this paper clearly illustrate the high potential of scanning transmission electron microscopy (STEM) analytical tools to unveil the finest structural details of complex catalytic materials.

Experimental Section

Two modified aluminas, kindly donated by Grace Davison, were used as supports of the mixed-oxide particles, an Al_2O_3-4 wt % La_2O_3 and an Al_2O_3-3.5 wt % SiO_2. BET surface areas were 181.61 m^2/g and 216 m^2/g, respectively. Ce and Pr, 25 wt %, were deposited onto both aluminas by incipient wetness impregnation using an aqueous solution containing a mixture of $Ce(NO_3)\cdot 3.6H_2O$ and $Pr(NO_3)\cdot 3.6H_2O$ in a 4:1 Ce/Pr molar ratio. After impregnation, the solids were dried in air overnight at 120 °C and then calcined at 500 °C during 6 h.

OSC was measured by oxygen consumption at 200 °C in a Micromeritcs ASAP-2020 volumetric adsorption device. Prior to the OSC measurements the samples were reduced for 1 h under 5% H_2/Ar flowing at 60 mL/min at selected temperatures, ranging from 200 to 900 °C. After reduction, the samples were evacuated, to remove traces of adsorbed hydrogen, for 1 h at the reduction temperature, except for those samples reduced below 500 °C, which were evacuated at 500 °C. The whole series of OSC measurements was carried out on the same sample, applying successive reduction treatments at increasing temperatures. Before starting the first catalyst reduction, the samples were preoxidized at 500 °C under 5% O_2/He during 1 h and further cooled down in oxygen to 125 °C.

(13) Rossignol, S.; Descorme, C.; Kappenstein, C.; Duprez, D. *J. Mater. Chem.* **2001**, *11* (10), 2587–2592.
(14) Church, J. S.; Cant, N. W.; Trimm, D. L. *Appl. Catal. A* **1993**, *101* (1), 105–116.
(15) Johnson, M. F. L. *J. Catal.* **1990**, *123* (1), 245–259.
(16) Arai, H.; Machida, M. *Appl. Catal. A* **1996**, *138* (2), 161–176.
(17) Rossignol, S.; Kappenstein, C. *Int. J. Inorg. Mater.* **2001**, *3* (1), 51–58.
(18) Navarro, R. M.; Alvarez-Galvan, M. C.; Rosa, F.; Fierro, J. L. G. *Appl. Catal. A* **2006**, *297* (1), 60–72.
(19) Miller, J. B.; Ko, E. I. *Catal. Today* **1998**, *43* (1−2), 51–67.
(20) Bernal, S.; Calvino, J. J.; Cifredo, G. A.; Finol, D.; Gatica, J. M.; Kiely, C. J.; Lopez-Cartes, C.; Zheng, J. G.; Vidal, H. *Chem. Mater.* **2002**, *14* (3), 1405–1410.
(21) Deganello, F.; Longo, A.; Martorana, A. *J. Solid State Chem.* **2003**, *175* (2), 289–298.
(22) Oudet, F.; Courtine, P.; Vejux, A. *J. Catal.* **1988**, *114* (1), 112–120.
(23) Wang, S. W.; Borisevich, A. Y.; Rashkeev, S. N.; Glazoff, M. V.; Sohlberg, K.; Pennycook, S. J.; Pantelides, S. T. *Nat. Mater.* **2004**, *3* (4), 274–274.
(24) Popa, A. F.; Rossignol, S.; Kappenstein, C. *J. Mater. Chem.* **2002**, *12* (10), 2866–2868.
(25) Aboussaïd, K.; Bernal, S.; Blanco, G.; Cifredo, G. A.; Galtayries, A.; Pintado, J. M.; Soussi el Begranib, M. *Surf. Interface Anal.* **2008**, *40*, 250–253.

For electron microscopy analysis, the samples were prepared by depositing a small amount of the powders directly onto lacey-carbon coated Cu grids. Excess powder was removed from the grids by gentle blowing with a nozzle. A JEOL2010F microscope, working at 200 kV, was used to characterize the samples. This instrument has a structural resolution of 0.19 nm, and it is equipped with a HAADF detector, an EELS spectrometer (GIF2000 Gatan Imaging Filter), and a X-EDS, Oxford INCA Energy 2000 system.

The structural characterization of the samples was performed by HREM, STEM-HAADF, and electron tomography. The chemical elements distribution was studied by combining HAADF images with the spectroscopy techniques X-EDS and EELS.

STEM-HAADF electron tomography[26] was conducted on a FEI TECNAI-F20 microscope operating at 200 kV using an ultrahigh tilt Fischione 2020 holder. The data collection was carried out by tilting the specimen about a single axis perpendicular to the electron beam. A series of projections was acquired every 2° from −74° to 74°. The tilt series was aligned and reconstructed using a SIRT algorithm in the FEI Inspect3D software.

To visualize a 3D model of the reconstruction, Amira 3.1 (Mercury) software was used to segment the data set manually, slice by slice, into discrete subvolumes corresponding to the catalyst support and Ce−Pr agglomerates. The contrast in each slice was sufficient to identify each component of the reconstruction by eye and enable the support and agglomerates to be surface rendered; this allows easy and informative visualization and to enable the surface area and volumes of the particles and support to be determined.

The chemical elements distribution was studied by combining HAADF images with X-EDS and EELS in STEM mode using a 0.5 nm probe size and a 10 cm camera length. The EELS spectra were recorded using the spot and spectrum imaging (SI) modes. The SI mode consists on acquiring a collection of spectra at successive positions separated by a distance slightly larger than the beam size (0.7 nm in our case) while the fine electron probe (0.5 nm in our experiments) is scanned over a predefined region in the sample. The HAADF signal is also collected at each point of the scan. This approach allows correlating nanoanalytical and structural information of the region under study. Spectra, with 0.3 eV energy dispersion, were recorded using an acquisition time of 3−5 s and convergence and collection semiangles of 8 and 24 mrad, respectively. Further element distribution information was gathered using energy filtered imaging (EFTEM). The EFTEM experiments were performed in a JEOL3010 microscope. This microscope is equipped with a LaB_6 filament, an HR-objective lens with chromatic and spherical aberration coefficient of 1.3 and 0.6 mm, respectively, and a point to point resolution of 0.17 nm. The instrument is also equipped with a GIF 200 EELS filter. To follow the spatial distribution of Al, La, Ce, and Pr, a series of EFTEM images covering the 30−200 eV (Al-L, La, Ce, and Pr N edges) and 790−1035 eV (La, Ce, and Pr M edges) ranges were acquired using a 5 eV slit. The images were recorded using acquisition times of 5 s (Al) and 20 s (La, Ce, Pr) and convergence and collection semiangles of 12.5 and 25 mrad for the La-doped sample. In the case of the Si-doped sample the Al, Si, Ce, and Pr distribution was determined by acquiring series of EFTEM images in the 50−198 eV and 825−1027 eV ranges using a 2 eV slit. The images were recorded using acquisitions time of 5 s and 20 s and a convergence and collection semiangle of 7.5 and 15 mrad. A homemade script was used to measure the image drift and to generate the Spectrum Imaging-EFTEM Data Cube. From these EFTEM data cubes a complete EELS spectrum can be extracted from each point in the image.[27]

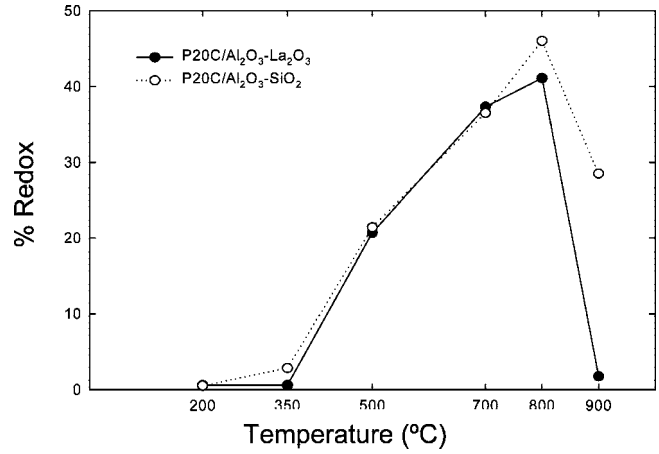

Figure 1. OSC in terms of the reduced percentage of Si- and La-doped samples.

The quantification of lanthanide elements from EELS spectra was carried out analyzing the M_5 and M_4 lines of La, Ce, and Pr, which appear in the 830−950 eV energy-loss range. The Pr-M_5 and Ce-M_4 lines overlap, and the lack of precisely determined Ce-$M_{4,5}$ and Pr-$M_{4,5}$ cross sections makes quantification a delicate task. In our case, a power law model, using a window width of 10 eV, was used to remove the background beneath La $M_{4,5}$, Ce-$M_{4,5}$, and Pr-$M_{4,5}$. The M-edge element cross sections were calculated using the Hartree-Slater model and the Ce/Pr and La/Pr atomic ratios were calculated using a 20 eV window width for the signal integration. A similar procedure was followed to construct the EFTEM elemental maps.

Simulated HREM images have been obtained using the Multislice and image formation process routines of JEMS software.[28]

XPS measurements were performed on samples reduced 1 h under a H_2 (5%)/Ar flow at selected temperatures from 350 to 900 °C and then reoxidized at 200 °C under flowing O_2(5%)/He before exposing them to the atmosphere. XPS data were recorded using a Kratos Axis Ultra DLD spectrometer, equipped with monochromatic Al Kα radiation at 1486.6 eV and a 2 × 1 mm spot size for all analyses. A 20 eV pass energy was used to collect the spectra. The powder samples were pressed into pellets and analyzed without any further treatment. The binding energy (BE) scale was calibrated by measuring the highest BE peak (u''' peak) for Ce 3d spectra at 917.0 eV.[29]When the u''' peak was too small because of the high reduction degree of the samples, the Ce^{3+} highest BE peak at 904.2 eV was used as reference (u' peak).

Results and Discussion

The redox properties of the $Ce_{0.8}Pr_{0.2}O_{2-x}/Al_2O_3$-3.5% SiO_2 (from now named as Si-doped sample) and $Ce_{0.8}Pr_{0.2}O_{2-x}/Al_2O_3$−4% La_2O_3 (La-doped sample) were obtained by measuring their OSC. Figure 1 shows the OSC in terms of the percentage of reduced mixed oxide. In both samples, we observe that OSC increases from 200 to 800 °C followed by a steep decrease at 900 °C. Both samples have a similar

(26) Midgley, P. A.; Weyland, M. *Ultramicroscopy* **2003**, *96* (3−4), 413–431.
(27) Bayle-Guillemaud, P.; Radtke, G.; Sennour, M. *J. Microsc. (Oxford, U.K.)* **2003**, *210*, 66–73.
(28) Stadelmann, P. *Microsc. Microanal.* **2003**, *9* (Suppl. 03), 60–61.
(29) Holgado, J. P.; Alvarez, R.; Munuera, G. *Appl. Surf. Sci.* **2000**, *161* (3−4), 301–315.

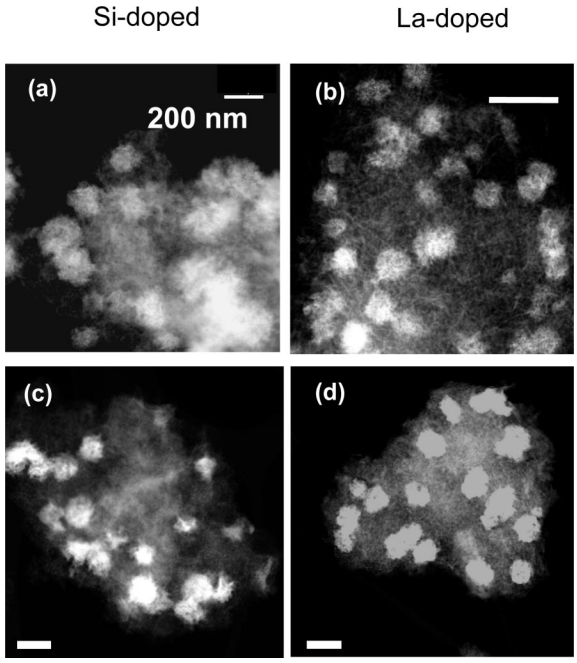

Figure 2. Medium magnification STEM HAADF images of the (a) Si-doped at 350 °C; (b) La-doped at 350 °C; (c) Si-doped at 900 °C; and (d) La-doped at 900 °C.

behavior in the 350−700 °C range, but the Si-doped sample shows a much better performance at high temperatures, 800−900 °C. Thus, the La-doped sample presents an abrupt decay of its OSC to a null value at 900 °C whereas the Si-doped one still retains a significant redox activity at this temperature (70% of initial value). These variations must be correlated with the details of their structure.

Structural Characterization. The ternary systems investigated here are rather complex with respect to their composition. For this reason, we have used HAADF imaging to obtain, in a first approach, a rough picture of the spatial distribution of the different components, that is, the mixed oxide and the alumina support. Figure 2 illustrates medium magnification HAADF images of the Si- and La-doped samples treated in H_2 at 350 °C, Figure 2a,b, and 900 °C, Figure 2c,d. Taking into account that the HAADF signal is proportional approximately to the average value of Z^2, where Z is the atomic number,[30] the high intensity areas observed in these images must correspond to the component which incorporates high atomic number elements, that is, the lanthanide mixed oxide, and the low intensity areas will correspond to the alumina support. With this consideration, the average size (diameter) of the mixed oxide aggregates which can be estimated from these images are 225 and 104 nm for the Si- and La-doped samples, respectively. Increasing the reduction temperature from 350 to 900 °C does not significantly modify the size of the supported mixed oxide aggregates in the case of the Si-doped sample but induces the average size of these aggregates to grow up to about 210 nm in the La-doped catalyst.

Focusing on the regions of the images which can be assigned to the alumina support, it is important to remark that in the images of the Si-doped samples a faint contrast layer is observed in between the mixed oxide aggregates. This layer extends over large regions of the alumina

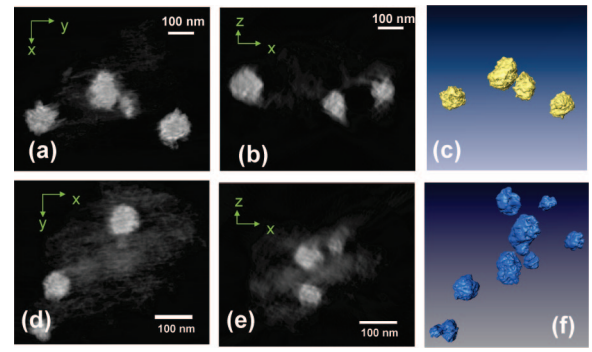

Figure 3. Mutually perpendicular slices through the reconstructed tomogram for the Si-doped sample (a, b) and La-doped sample (d, e) at 350 °C. Surface render of the tomographic reconstruction for the Si-doped sample (c) and the La-doped sample (f).

crystallites. This contrast feature, which is observed both in the images recorded after reduction at 350 °C and in those obtained on the 900 °C reduced sample, precludes at clear the observation of the alumina support. In contrast, the images obtained on the La-doped sample, depict much more clearly the fiber-like shape of the alumina crystallites.

To obtain additional information on the shape and morphology of the mixed oxide aggregates, as well as to identify the support/aggregate interface, electron tomography has been performed on the Si-doped and La-doped samples, see Figure 3. This analysis was focused on the low temperature samples because our goal has been to understand the origin of differences in the high temperature OSC values. As deduced from the tomography results in Figure 3, there are some similarities between samples; (i) the mixed oxide aggregates have a 3D morphology with a rough surface as observed in the reconstruction and the reprojected images in Figures 3c,f; (ii) the aggregates are physically mixed with the alumina support as seen in the orthogonal slices of the reconstructed tomogram in Figure 3a,b,d,e; and (iii) the aggregates are dispersed all over the alumina support. Segmentation of the mixed oxide particles from the tomograms has allowed us to estimate some morphological parameters, in particular their volumes. A comparison of the two samples indicates that the mixed oxide particles are significantly larger in the catalyst prepared on the SiO_2-doped support. Thus, if the size of each particle is expressed as the radius of the sphere with the same volume as the particle, the average values of the radii observed in the two catalysts are the following: 55 nm for the catalyst based on SiO_2 and 33 nm for that based on La_2O_3. In good agreement with HAADF images, the mixed oxide aggregates are, on average, larger in the former catalyst.

The structure of the large-size aggregates observed in the HAADF images was studied by HREM. Figure 4a,b shows representative HREM images of the high intensity regions observed in the Si-doped and La-doped samples, respectively, after reduction at 350 °C. A first observation of the images indicates the crystalline nature of these regions. A crystallographic analysis of these images by Fourier transforms techniques (see diffractograms shown as insets) indicates the

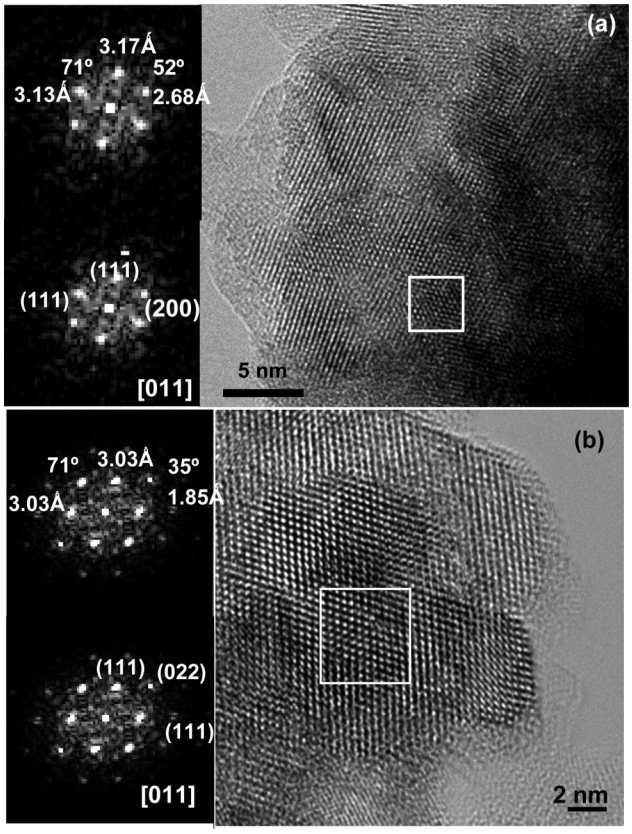

Figure 4. Experimental HREM image acquired on the (a) Si-doped and (b) La-doped samples reduced at 350 °C. Images were acquired from the areas of high HAADF intensity shown in Figure 2a,b.

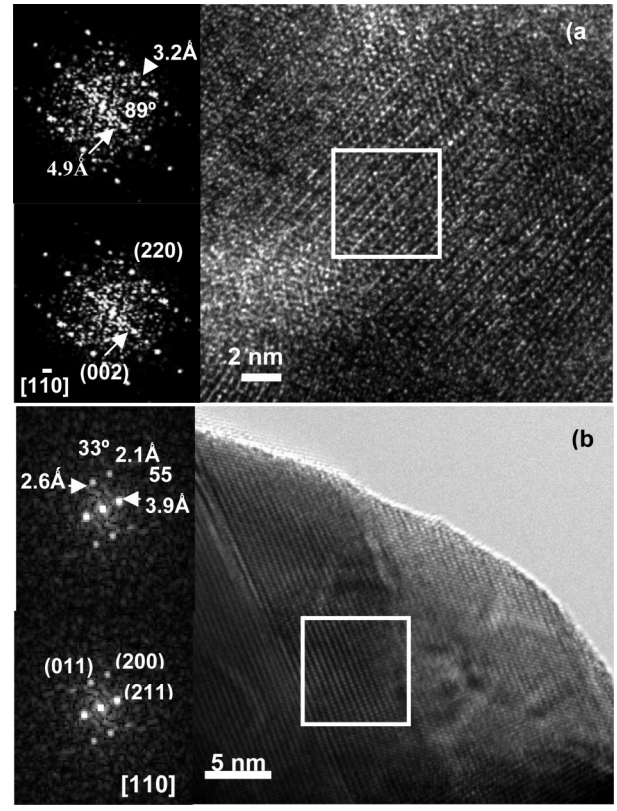

Figure 5. Experimental HREM image acquired on the (a) Si-doped and (b) La-doped samples reduced at 900 °C. Images were acquired from the areas of high HAADF intensity shown in Figure 2c,d.

presence of a fluorite structure with lattice parameters close to those characteristic of cerium dioxide.[31] In particular, Figure 4a,b shows (002) and (111) reflections of the [011] orientation of ceria. Images along the [100], [111], and [112] orientations, which are all that can be recorded for a fluorite structure with lattice parameters in the order of those of ceria within the resolution limit of the microscope we have used, were also recorded. These results confirm the previous interpretation of the HAADF observations, according to which the high intensity regions corresponded to the mixed oxide crystals. HREM analysis indicates, therefore, that both Si- and La-doped samples reduced at 350 °C contain crystallites of a fluorite structure which in principle would incorporate Ce and Pr. This fact would explain their similar OSC behavior at low temperature.

After reduction at high temperature, HREM reveals a quite different structure of the large sized, lanthanide element containing aggregates between the two catalysts, Figure 5. The angles and distances measured on the images of the Si-doped sample, Figure 5a, differ significantly from those determined for the La-doped catalyst, Figure 5b. This confirms the presence of different crystalline phases in both materials. A detailed analysis of Figure 5a indicates the presence of two crystalline phases at the Si-doped sample; a cubic, fluorite type, phase and a lanthanum hydroxycarbonate ($LnOHCO_3$) phase. The latter could be the result of the exposure to air of a cerium sesquioxide phase. It is well-known[32] that the reduction of CeO_2 at high temperature may lead to phases with a reduction degree close to 100%, that is, to a sesquioxide Ce_2O_3 phase. If the reduction temperature is sufficiently high, a transformation from the cubic to the hexagonal phase can take place. As reported in ref 33, when this hexagonal sesquioxide is exposed to air, two successive processes take place; first, the hydration and carbonation of the sesquioxide, which generates a hydroxycarbonate, and second, the dismutation of the hydroxycarbonate toward cerium dioxide, CO_2 and H_2. This would explain the presence of these two phases in this sample. In particular, the image in Figure 5a shows lattice spacings characteristic of a crystalline hydroxycarbonate phase. In the case of lanthanide hydroxycarbonates, $LnOHCO_3$, two different polymorphs are known; an orthorombic phase, called Ancilite,[34] and a hexagonal structure, Bastnesite.[35] To identify the crystalline hydroxycarbonate phase in our catalysts, diffraction patterns of the ancilite and hexagonal bastnesite phases at different orientations were simulated. Comparing the simulated diffraction patterns with the Fourier transforms of experimental HREM images, we could rule out the orthorhombic phase (Ancilite). Additionally, to confirm the presence of the bastnesite polymorph we calculated a thickness-defocus map for the crystallographic orientation of this phase which

(30) Pennycook, S. J.; Jesson, D. E. *Ultramicroscopy* **1991**, *37* (1−4), 14–38.
(31) Trovarelli, A. *Catalysisi by ceria and Related Materials*; Imperial College Press: London, 2002; Vol. 2.
(32) Pintado Caña, J. M. Ph.D. Thesis, Universidad de Cádiz, Cádiz, 1995.
(33) Bernal, G. B. S.; Gatica, J. M.; Pintado, J. M.; Pérez-Omily, S. *Boletín de la Sociedad Española de Cerámica y Vidrio* **1997**, *36* (2−3).
(34) Dexpert, H.; Caro, P. *Mater. Res. Bull.* **1974**, *9* (11), 1577–1585.
(35) Christensen, N. *Acta Chem. Scand.* **1973**, *1* (27), 2973–2982.

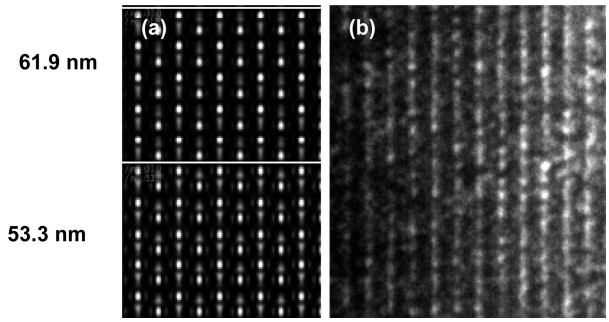

Figure 6. (a) Two HREM simulated images extracted from a thickness-defocus map of Bastnesite phase at the [011] zone axis with a defocus equal to −40 nm and a voltage acceleration of 200 kV. The images were simulated using the following parameters C_s = 0.5 mm, objective lens aperture diameter = 12 nm^{-1}, focal spread = 10 nm, and accelerating voltage = 200 kV. (b) Experimental HREM image.

matched the features of the Fourier transform. Figure 6 illustrates an experimental HREM image and two HREM simulated images extracted from this thickness-defocus map. Note that there is a good agreement between the contrasts in these images. Therefore, these results indicate that in the case of the Si-doped sample, after reduction at high temperature the large lanthanide containing aggregates become fully reduced.

The response against a high temperature treatment of the La-doped sample is neatly different. HREM images recorded on this sample show very different contrast patterns, Figure 5b. The analysis of the diffractograms of these images indicates the formation of a perovskite type $LnAlO_3$ phase. This has been confirmed by HREM image simulation. The perovskite phase is formed as a result of a solid state reaction between the mixed oxide and the La-doped alumina, possibly by diffusion of Al and La into the cerium−praseodymium mixed oxide structure. The stabilization of the +3 oxidation state of Ce and Pr within this phase prevents their reoxidation. This blockage of the Ln^{4+}/Ln^{3+} redox couple would explain the OSC decline observed experimentally at these temperatures.

In the case of the Si-doped sample treated at 900 °C, the perovskite phase has also been observed by X-ray diffraction.[25] Such a phase could not be identified in the HREM studies. This suggests that the perovskite phase accumulates in the thicker, non-electron-transparent areas of the sample where HREM analysis cannot be performed, very likely at the core of the micrometer sized aggregates detected in the HAADF images, Figure 2. The presence of such a fraction of perovskite phase would be also responsible of the OSC decline observed in the Si-doped sample at high temperature. The presence of fluorite type structures in the Si-doped samples would explain the higher values of OSC.

These differences in the nanostructure of the two catalysts suggest that silicon could block the mixing of cerium and praseodymium with the alumina substrate. Such an effect would prevent the formation of the perovskite phase, which is responsible for the redox-activity decay at high temperature. With this idea in mind, we found of major interest to investigate the detailed distribution of the different lanthanide elements present in these catalysts as a function of reduction temperature.

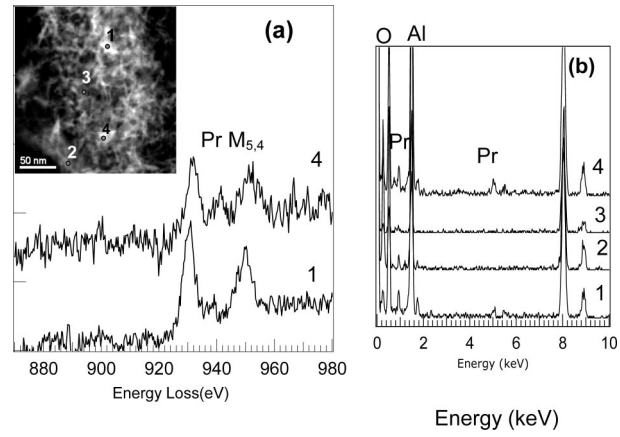

Figure 7. (a) EELS and (b) X-EDS spectra acquired on the alumina support of the Si-doped samples (displayed on the inset HAADF figure) at points 1−4.

Nanoanalytical Characterization. HREM has provided definite clues about the relationship between the formation of a perovskite phase and the redox deactivation process, and HAADF images have allowed a gross picture about the element distribution in the two catalysts to be obtained. STEM-XEDS, STEM-EELS, and EFTEM investigations were performed to obtain some evidence about the role of the alumina dopants on the high temperature OSC behavior.

Si-Doped Samples. Figure 7 illustrates a representative analysis carried out on different positions of the substrate of the Si-doped sample reduced at 350 °C, that is, outside the large aggregates detected by HAADF. EELS and X-EDS analysis, Figure 7a,b, were performed in STEM mode using a 0.5 nm electron beam probe diameter. It is important to remark that points 1 and 4 correspond to areas with a high HAADF intensity within the substrate. EELS spectra corresponding to positions 1 and 4 show only a characteristic signal at 931−950 eV. Such a signal corresponds to the $M_{4,5}$ lines of Pr. In positions 2 and 3 no signal is detected in the energy loss region characteristic of the lanthanide elements (Ce, Pr). Such a result indicates the presence of Pr rich areas on high HAADF intensity regions of the substrate. Similar results have been found with X-EDS, Figure 7b. The X-EDS spectra, in the 0−10 keV energy region, were acquired simultaneously with EELS spectra at points 1−4. All X-EDS spectra show signals corresponding to K transitions of O (0.4 keV), Al (1.5 keV), Si (1.9 keV), and Cu (8.1 keV). In addition, L and M transitions Pr-L (0.9 KeV) and Pr-M (5.1 KeV) are also observed at points 1 and 4 as previously observed by EELS. The observed Cu signal is not due to the sample but to excitations of both the Cu grid on which the sample is mounted for observation as well as from the microscope itself. The Al and Si signals come, as expected, from the support crystallites. This result demonstrates that a fraction of praseodymium used for the synthesis process does not mix with cerium during the catalyst preparation but, instead, remains isolated in direct contact with the Si-doped substrate in the form of pretty small regions, just a few nanometres.

To confirm these observations and to estimate the size of the Pr-rich domains, spatially resolved EELS was performed

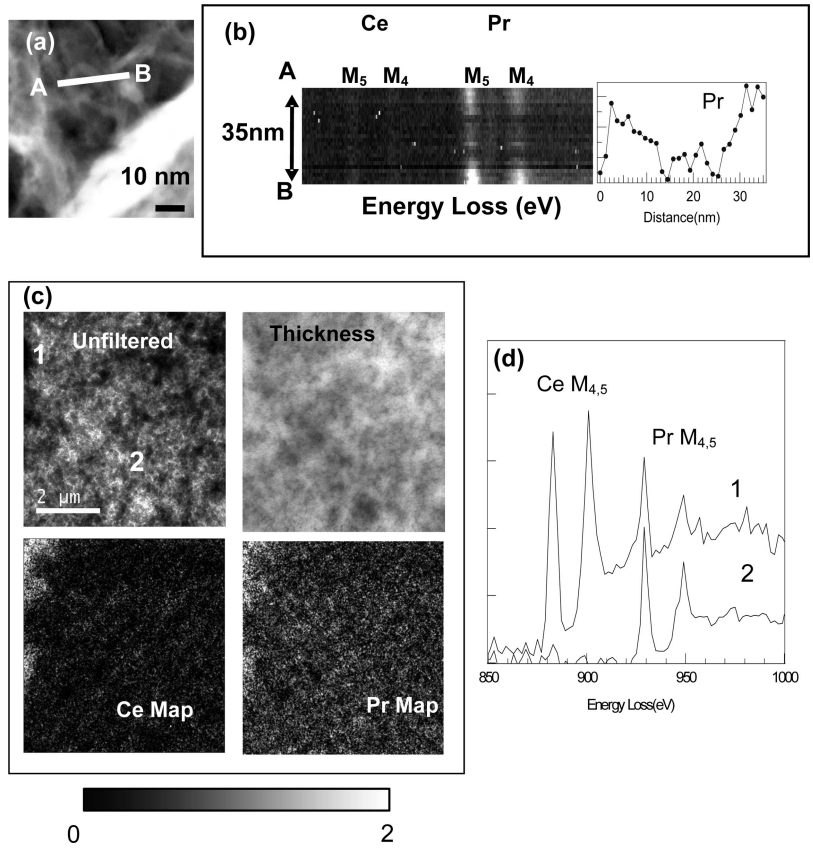

Figure 8. (a) HAADF image of the support area of the Si-doped at 350 °C, (b) gray scale and Pr intensity profile image of the EELS-SI performed along the A-B line (displayed in part a). (c) EFTEM images of the Si-doped sample and (d) EELS spectra corresponding to 1 and 2 extracted from the EFTEM Data Cube.

using the spectrum-imaging mode (SI-EELS). Figure 8a,b illustrate a SI-EELS analysis acquired along a 35 nm line path, marked as A−B on the HAADF image, Figure 8a. Figure 8b shows the result of this EELS spectrum-line record in the form of a gray scale image. The position of the Ce and Pr signals in the energy scale has been marked. Note how only the Pr-$M_{4,5}$ signals (931−950 eV) flash out, in a discontinuous fashion, along the analyzed path, whereas no signal due to cerium is observed. Thus, the Pr signal is observed from the beginning of the line (point A) up to a 13.5 nm distance. At this point the signal vanishes and reappears again at 19.5 nm (at the position marked with a white arrow on the SI image). Pr peaks are then observed from 19.5−23.3 nm and 27.2−35 nm (point B). This result confirms the presence of small praseodymium-containing regions on the alumina support. As estimated from the SI-EELS analysis, the Pr-containing regions size is in the 5−15 nm range. A wide view of the Pr distribution has been obtained through the EFTEM analysis performed on the Si-doped sample at 350 °C, Figure 8c,d. Ce and Pr maps (Figure 8c) indicate the presence of Ce−Pr aggregates and the presence of Pr domains dispersed on the alumina support. Figure 8d shows EELS spectra extracted from the EFTEM Data Cube. The spectrum corresponding to area 1 shows Ce and Pr $M_{4,5}$ edges while the spectrum from area 2 (Pr domain on the alumina support) only displays the Pr $M_{4,5}$ edge.

In the case of the Si-doped sample treated at 900 °C, EELS and X-EDS analysis was performed on the large crystals

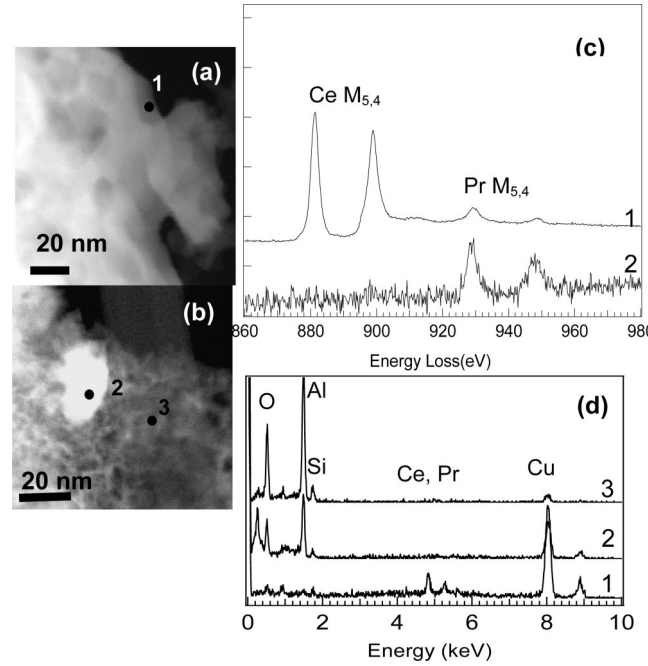

Figure 9. HAADF images acquired on a large crystal (a) and a small crystal supported (b) on the Si-doped sample at 900 °C. EELS (c) and X-EDS spectra (d) obtained from points 1−3.

(Figure 9a, point 1), previously identified by HREM as hydroxycarbonate-like or fluorite-like phases, but also on the small crystals (Figure 9b, point 2) and the alumina substrate (Figure 9b, point 3). EELS spectra acquired on large crystals

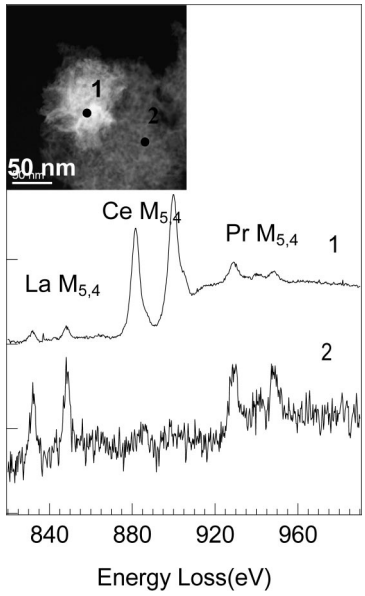

Figure 10. EELS spectra acquired on points 1 and 2 (HAADF image inset) on the La-doped sample at 350 °C.

(Figure 9c, point 1), shows the characteristic Ce-$M_{4,5}$ (881.4−899.8 eV) and Pr-$M_{4,5}$ (931−950 eV) signals. A quantification of the spectrum indicates that the crystal is 90% Ce and 10% Pr, values slightly higher than the nominal values (80% Ce and 20% Pr). The X-EDS spectrum, from the same area (Figure 9d, point 1), indicates the presence of only these elements in these large aggregates. In good agreement with previous HREM data, these results confirm that these particles correspond to phases that only contain, in addition to oxygen, cerium and praseodymium, EELS spectra from the small crystallites, in this case a 20 nm crystal (Figure 9b, point 2), show the characteristic Pr-$M_{4,5}$ (931−950 eV) signals. X-EDS spectra acquired in the same area (Figure 9d, point 2) also show the Al and Si signals, which come from the underlying support. EELS and X-EDS analysis performed on the alumina substrate (Figure 9b, point 3) indicates the absence of Pr. These results confirm the presence of praseodymium rich crystals with a size in the 20−30 nm range in the Si-doped sample at 900 °C. These crystals very likely come from those observed after reduction at 350 °C, the size increase due to sintering.

The nanoanalytical study performed on Si-doped samples can be summarized as follows: (1) During the synthesis of the catalyst, Ce and Pr do not mix completely, and a fraction of the praseodymium loading remains as separate nanosized particles. The size of these Pr-containing particles depends on the reduction temperature; (2) the substrate is made of Al, Si, and O; (3) cerium concentrates in very large particles mixed with praseodymium but in a Ce/Pr ratio higher than that targeted in the synthesis; and (4) the spatial distribution of the elements is not affected by increasing the reduction temperature.

La-Doped Samples. The spectroscopic studies on the La-doped sample provided results very different to those observed on the Si-doped samples. Figure 10 displays representative EELS spectra acquired on the La-doped sample treated at 350 °C. EELS spectrum 1, acquired on a high intensity HAADF region (inset, Figure 10, point 1), shows the characteristic $M_{4,5}$ La, Ce, and Pr signals (832−842 eV, 881−900 eV, and 931−950 eV, respectively). At the lower intensity HAADF regions (inset Figure 10, point 2), only La and Pr could be detected; see spectrum 2, Figure 10. A series of analyses on different areas of the substrate indicates that Pr is homogeneously distributed on the alumina substrate. The results have been confirmed using EFTEM imaging where a wider view of the sample is analyzed. Figure 11 displays the unfiltered image, the thickness map, and the Al, La, Pr, and Ce chemical maps. As observed from the images, Pr is homogeneously distributed on the alumina support. The EELS spectra extracted from the EFTEM Data Cube, Figure 11b, shows the presence of La, Ce, and Pr on area 1 where a mixed oxide aggregate is present, and there are only La and Pr signals on area 2, which corresponds to the alumina support.

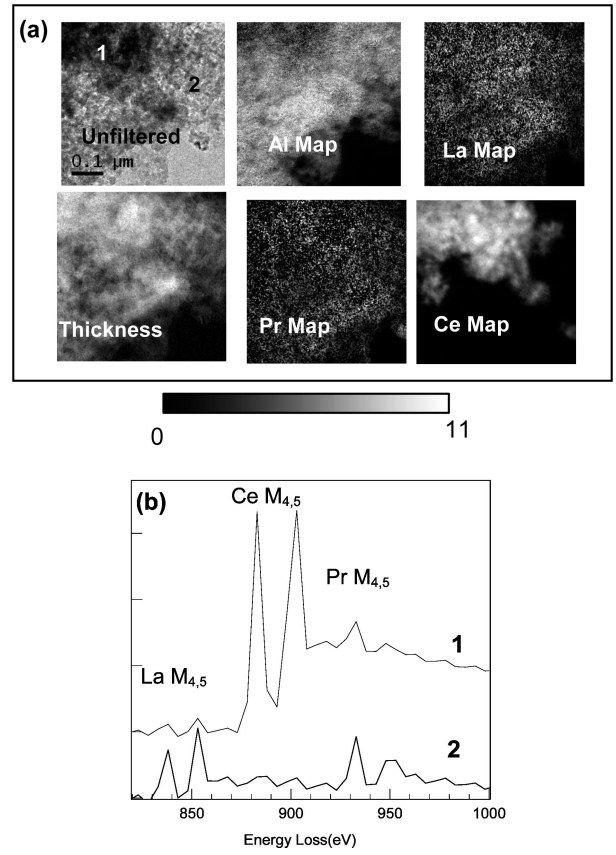

Figure 11. EFTEM analysis on the La-doped sample at 350 °C. (a) Unfiltered image of the analyzed area and thickness, Al, La, Pr, and Ce maps extracted from the EFTEM analysis. (b) EELS spectra extracted from the EFTEM Cube data, corresponding to areas 1 and 2.

Similar results were found on the La-doped sample after reduction at 900 °C. The results of SI-EELS experiments performed on the sample are depicted in Figure 12. In this case 50 spectra and its corresponding HAADF signal were simultaneously acquired while the beam was scanned along a 127 nm line, going from A to B in Figure 12a, with a step size of 2.5 nm. Two spectra extracted from the whole set, corresponding to points 1 and 2 (Figure 12a), are displayed in Figure 12b. EELS spectrum from point 1, located on a high HAADF intensity area, contains signals of La, Ce, and Pr. In contrast, in spectrum 2, corresponding to a lower

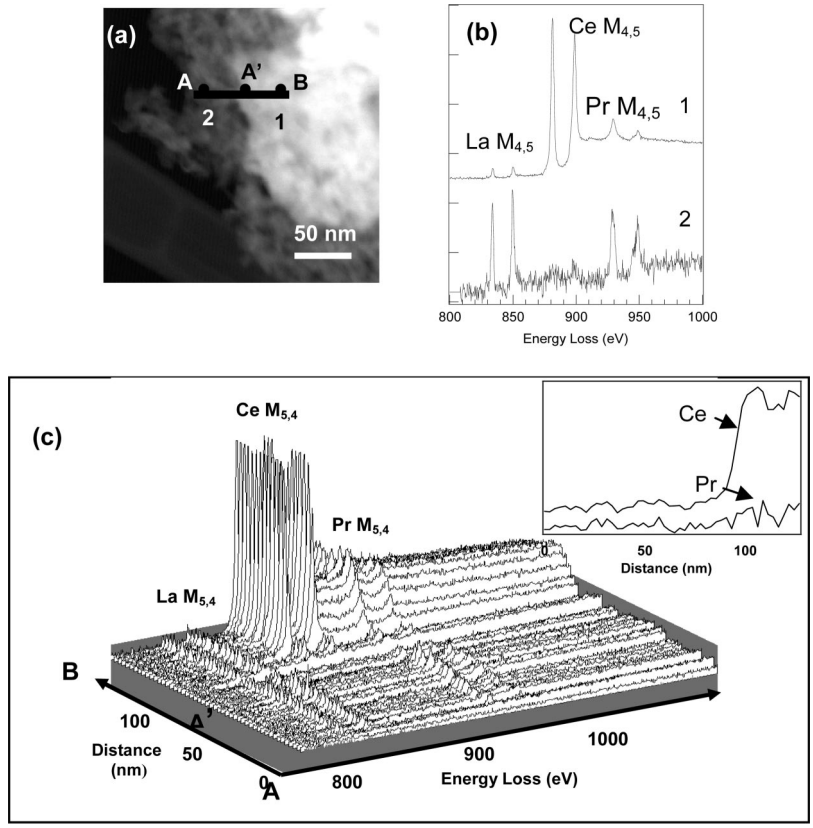

Figure 12. (a) HAADF image of the La-doped sample at 900 °C. (b) EELS spectra 1 and 2 extracted from the SI-EELS analysis. (c) EELS 3D representation of a collection of 50 spectra acquired along the A-B line, A′ indicates the crystal-substrate interface and inset image including the Ce and Pr intensity profile along the A−B line.

Table 1. EELS Quantification Data from the La-Doped Sample at 350 °C and 900 °C[a]

La-doped sample at 350 °C				La-doped sample at 900 °C			
La at. %	Ce at. %	Pr at. % total	Ce/Pr*	La at. %	Ce at. %	Pr at. % total	Ce/Pr*
3.9	80.9	15.3(10.3+5.1)*	7.9	4.3	80.3	15.5(10.8+4.7)*	7.4
8.9	75.6	15.5(4.0+11.5)*	19.1	4.8	82.7	12.5(7.3+5.2)*	11.4
4.5	82.0	13.3(7.5+5.8)*	11.0	5.9	78.9	15.3(8.8+6.5)*	9.0
4.2	79.1	16.6(11.2+5.5)*	7.1	7.4	79.5	13.1(5.0+8.1)*	16.0
9.0	61.8	29.2(17.5+11.7)*	3.5	4.1	80.4	15.5(11.0 +4.5)*	7.3
13.3	66.6	20.1(2.8+17.3)*	23.4	3.9	77.6	18.5(14.3+4.2)*	5.4
6.7	82.3	11.0(2.3+8.7)*	36.1	5.2	74.7	20.1(14.4+5.7)*	5.2

[a] The Ce/Pr* values have been corrected taking into account only the Pr present on the cerium mixed oxides. *(Pr crystal + Pr support) where % Pr crystal = % Pr total − [% La/(Pr/La ratio)]; % Pr support = % Pr total − % Pr crystal.

HAADF intensity region, only the La and Pr signals are observed. A detailed picture of the distribution of La, Ce, and Pr along the A−B line can be obtained from the analysis of the 3D representation of the whole collection of EELS spectra (Figure 12c). In this figure, Pr and La $M_{4,5}$ signals are observed from point A up to a distance of 77 nm (indicated as A′). At this point the Ce-$M_{4,5}$ signals peak out. This occurs exactly at the border of the high HAADF intensity area, that is, when we are entering one of the large size aggregates.

These results clearly evidence a homogeneous distribution of Pr on the substrate of this La-doped sample, similar results being observed after reduction at either 350 or 900 °C.

To evaluate more accurately the element distribution in the two distinct parts of this material, that is, the support particles and the large aggregates containing Ce and Pr, a detailed quantification of the EELS spectra was carried out. Table 1 gathers quantification results obtained from a series of spectra acquired at different areas of the La-doped sample treated at 350 °C. The La, Ce, and Pr atomic % and the Ce/Pr atomic ratios are displayed. The estimation of the La and Pr percent in substrate areas is straightforward. A very homogeneous distribution of these elements, in a more or less constant La/Pr ratio of about 0.8, was found in the substrate. The estimation of La, Ce, and Pr content within the large crystallites needs a more detailed consideration because in most cases the spectra were collected from locations where these crystallites overlap with those of the substrate. Hence, to estimate the Ce/Pr ratio into the large crystals, the Pr signal coming from the underlying substrate needs to be previously removed. To eliminate the contribution of the Pr signal coming from the support, the intensity of the La peaks was measured, and a La/Pr atomic ratio of 0.8 was applied. Taking into account such a correction, the Pr content into the mixed oxide crystal and the Ce/Pr atomic

Table 2. EELS Quantification Data from the Si-Doped Samples at 350 °C and 900 °C

Si-doped sample at 350 °C			Si-doped sample at 900 °C		
Ce at. %	Pr at. %	Ce/Pr	Ce at. %	Pr at. %	Ce/Pr
86.0	14.1	6.1	90.3	9.7	9.3
93.1	6.9	13.4	71.6	28.4	2.5
84.1	15.9	5.3	91.0	8.0	11.3
71.4	28.7	2.5	82.3	18.7	4.4
87.4	12.6	6.9	82.7	17.4	4.7

Table 3. XPS Quantification Data from the Samples Reduced at 350 °C and 900 °C

	Si-doped		La-doped	
reduction temperature (°C)	Ce 3d/ Pr 3d	(Ce 3d+Pr 3d)/ Al 2p	Ce 3d/ Pr 3d	(Ce 3d+Pr 3d)/ Al 2p
350	0.55	0.036	0.81	0.042
900	0.54	0.037	0.77	0.051

ratio were estimated, Table 1. We observe that the Ce/Pr ratio values present a strong variation, going from 3.5 up to 36.1. Table 1 also displays the results obtained for the La-doped sample reduced at 900 °C following the same procedure. In this sample the La/Pr atomic ratio outside the large crystallites was estimated to be 0.9 and the Ce/Pr atomic ratios fall now in the 5.2−16.0 range.

In this case, Pr is not homogeneously distributed onto the substrate, and so the observed Pr corresponds only to that incorporated either within the large Ce−Pr mixed oxide aggregates or that present in the Ce-free, Pr-containing, small crystallites. The EELS quantification data obtained for the Ce mixed crystals of the Si-doped samples at both reduction temperatures are collected in Table 2. In these samples, the Ce/Pr atomic ratio ranges from 2.5 to 13.5, for the sample treated at 350 °C, and from 2.5 to 11.3, after reduction at high temperature.

Comparing these experimental values with the nominal Ce/Pr atomic ratio (Ce/Pr = 4 at.), we observe that for both doping systems (La_2O_3 and SiO_2) the actual Ce/Pr atomic ratio values are significantly different to the nominal value, the Ce/Pr range being much wider in the case of the La-doped samples. The deviation between these values is also higher in the La-doped material very likely because Pr has spread in a large extent all over the substrate, whereas only small amounts of Pr remain unmixed and keep more concentrated, as nanocrystals, in the case of the alumina doped with SiO_2. This feature of the praseodymium distribution is present in both materials at the lowest reduction temperature and does not change noticeably by increasing the reduction temperature. Therefore it seems to be a result of the synthesis procedure.

Average Surface Composition by XPS. A complementary characterization study by XPS was performed on the Si- and La-doped samples reduced at 350 and 900 °C. This technique will give us average information of the chemical composition of the samples. Furthermore, as XPS is a surface sensitive technique, the analysis will only involve elements from the outermost layers of material. Table 3 summarizes the quantitative results obtained for Si- and La-doped samples, respectively.

The Ce/Pr atomic ratios estimated for the samples reduced at 350 °C are well below the bulk nominal value (i.e., Ce/Pr = 4). This is in good agreement with the model depicted in this paper for the lanthanide elements distribution. Both Si-doped and La-doped samples show a nonhomogeneous distribution of Ce and Pr, a fraction of praseodymium remaining unmixed with cerium. This praseodymium is well dispersed over the surface of the alumina support, as small particles in the case of Si-doped sample, or more homogeneously distributed in the case of the La-doped system, being thus accessible to the XPS analysis depth. On the contrary, most of the cerium in the samples will be inaccessible to XPS, as it is found in large particles, ranging from 100 to 200 nm. In summary, most of the Pr is close to the surface, whereas only a small fraction of Ce will be analyzed by XPS, resulting thus in a low Ce/Pr ratio.

Another remarkable point is the different Ce/Pr ratio found for Si and La-doped samples. The lower Ce/Pr ratio observed by XPS in the Si-doped catalyst suggests a larger average size of the mixed oxide aggregates, as previously shown by HAADF and electron tomography.

After reduction at 900 °C, there are no dramatic changes in the Ce/Pr ratio. This observation is in good agreement with the nanoanalytical study, which suggested that the spatial distribution of the elements was not affected by the reduction treatment.

However, although the global distribution of lanthanide elements remains virtually unaltered after the reduction treatments, changes in the aggregate sizes should occur. The (Ce+Pr)/Al ratio reported in Table 3 gives information about the overall dispersion of the lanthanide elements. The higher the element ratio, the smaller the particle sizes containing Ce and/or Pr. Thus, sintering of the particles will result in a decrease of this element ratio. In the case of Si-doped sample, there is not significant change in the (Ce+Pr)/Al ratio, which indicates that little sintering of the particles should occur after reduction at 900 °C. Surprisingly, for the La-doped catalyst, a significant increase of the (Ce+Pr)/Al ratio was observed. The formation of the perovskite phase after reduction at 900 °C, as observed by HREM (Figure 4b), implies the diffusion of Al and La into the Ce/Pr mixed oxide particles, this driving large amounts of Al into the big $LnAlO_3$ aggregates. The fraction of Al located at the cores of these aggregates is out of reach for XPS analysis. This would allow understanding the increase in the (Ce+Pr)/Al ratio.

The observed evolution of (Ce+Pr)/Al ratios with reduction temperature reinforces the conclusions obtained by the nanostructural and nanoanalytical studies. Silicon should be blocking the mixing between Ce and Pr elements and the alumina support, and therefore, the element ratio (Ce+Pr)/Al remains constant, whereas the high affinity between alumina and the lanthanides should account for the incorporation of Al into the mixed oxide aggregates, which are much larger after the high temperature treatment. This would explain the increase of the (Ce+Pr)/Al ratio.

In summary, the whole set of results indicates that, independently of the doping agent (SiO_2 or La_2O_3) present in the substrate, part of the Pr loading used in the synthesis does not mix with cerium, this modifying the final Ce/Pr ratio of the resulting mixed oxide particles. The fate of the

unmixed Pr fraction is quite different in both materials, its distribution being deeply influenced by the nature of the doping agent. In the case of the material prepared on the La-doped substrate, praseodymium species do spread very efficiently all over the substrate, resulting in a very homogeneous situation. The presence of silicon in the substrate prevents such a homogeneous final situation. In this case, instead, the unmixed Pr fraction tends to agglomerate as nanoparticles which simply grow as reduction temperature is increased.

From a chemical perspective, these results clearly suggest a high affinity for the lanthanides in the La-doped substrate whereas such an affinity is greatly depressed when doping with silicon. This barrier effect to the incorporation of praseodymium within the alumina lattice must also work to prevent the formation of the $LnAlO_3$, redox inactive, perovskite phase. This lanthanide incorporation blockage will permit keeping the lanthanide ions in the framework of redox-active phases, being therefore responsible for the better resistance against OSC decay at high temperature observed in the catalyst prepared on the SiO_2-modified support. The origin of this lanthanide-phillic or lanthanide-phobic character, clearly evidenced in this nanostructural/nanochemical investigation, is actually a matter of further research in our laboratory.

Acknowledgment. We thank financial support from the Ministry of Science and Innovation of Spain/FEDER Program of the EU (Project MAT2008-00889/NAN) and the Junta de Andalucía (Groups FQM-110 and FQM-334). The authors acknowledge financial support from the European Union under the Framework 6 program under a contract for an Integrated Infrastructure Initiative. Reference 026019 ESTEEM. S.T. acknowledges the MEC "Ramón y Cajal" and "Jose Castillejo" Programs. The Electron Microscopy Division of SCCYT at Cadiz University is also acknowledged.

CM8029054